

Relativistic Mean Field Approximation to the Analysis of $^{16}\text{O}(e, e'p)^{15}\text{N}$ data at $|Q^2| \leq 0.4$ (GeV/c) 2

J.M. Udías¹, J.A. Caballero^{2,3}, E. Moya de Guerra³, Javier R. Vignote¹, A. Escuderos³

¹Departamento de Física Atómica, Molecular y Nuclear, Universidad Complutense de Madrid, E-28040 Madrid, Spain

²Departamento de Física Atómica, Molecular y Nuclear, Universidad de Sevilla, Apdo. 1065, E-41080 Sevilla, Spain

³Instituto de Estructura de la Materia, CSIC Serrano 123, E-28006 Madrid, Spain

Abstract

We use the relativistic distorted wave impulse approximation to analyze data on $^{16}\text{O}(e, e'p)^{15}\text{N}$ at $|Q^2| \leq 0.4$ (GeV/c) 2 that were obtained by different groups and seemed controversial. Results for differential cross-sections, response functions and A_{TL} asymmetry are discussed and compared to different sets of experimental data for proton knockout from $p_{1/2}$ and $p_{3/2}$ shells in ^{16}O . We compare with a nonrelativistic approach to better identify relativistic effects. The present relativistic approach is found to accommodate most of the discrepancy between data from different groups, smoothing a long standing controversy.

PACS: 25.30.Fj; 25.30.Rw; 24.10.-i; 21.60.Cs

Keywords: Quasielastic electron scattering; Negative-energy components; Response functions; Left-right asymmetry; Relativistic current.

I. INTRODUCTION

Quasielastic ($e, e'p$) processes are a powerful tool to study bound nucleon properties. Indeed, coincidence ($e, e'p$) measurements at quasielastic kinematics have provided over the years detailed information on the energies, momentum distributions and spectroscopic factors of bound nucleons. This is so because at quasielastic kinematics the ($e, e'p$) reaction can be treated with confidence in the impulse approximation, *i.e.*, assuming that the detected knockout proton absorbs the whole momentum (q) and energy (ω) of the exchanged photon (for recent reviews of the subject see ref. [1] and references therein). Until recently most data were concentrated in the low missing momentum range $p_m \leq 300$ MeV/c, where p_m is the recoil momentum of the residual nucleus. In the last years [2] higher p_m -regions are being probed at small missing energies E_m to study further aspects of bound nucleon dynamics and nucleon currents. A substantial amount of theoretical work on ($e, e'p$) has been carried out on the basis of nonrelativistic approximations to the nucleon current. This is the case of the standard distorted wave impulse approximation (DWIA) [1] that uses a nonrelativistic approximation to the nucleon current operator and wave functions. DWIA has been successfully used over the years [3] to analyze ($e, e'p$) data using bound and scattered proton wave functions deduced from phenomenological nonrelativistic potentials. The limits of validity of the nonrelativistic DWIA approach are now being studied by Meucci, Giusti and Pacati [4], among others.

In past years we investigated [5–8] nuclear responses and differential cross-sections for exclusive quasielastic electron scattering within the framework of relativistic mean field approximations. In the relativistic distorted wave impulse approximation (RDWIA) [5,9–11] the one-body nucleon current,

$$J_N^\mu(\omega, \vec{q}) = \int d\vec{p} \bar{\psi}_F(\vec{p} + \vec{q}) \hat{J}_N^\mu(\omega, \vec{q}) \psi_B(\vec{p}), \quad (1)$$

is calculated with relativistic ψ_B and ψ_F wave functions for initial bound and final outgoing nucleons, respectively, and with relativistic nucleon current operator, \hat{J}_N^μ . The bound state wave function is a four-spinor with well-defined parity and angular momentum quantum numbers, and is obtained by solving the Dirac equation with scalar-vector (S-V) potentials determined through a Hartree procedure from a relativistic Lagrangian with scalar and vector meson terms [12]. The wave function for the outgoing proton is a solution of the Dirac equation containing S-V global optical potentials [13] for a nucleon scattered with asymptotic momentum \vec{p}_F . Dirac equations for both scattered and bound wave functions are solved in coordinate space and their solutions are then transformed to momentum space where necessary.

Eq. (1) sets up the scenario where differences between RDWIA and DWIA are at play. To go from the relativistic to the nonrelativistic approach the one-body (4×4 matrix) current operator is first of all expanded in a basis of free nucleon plane waves. This amounts to a truncation of the nucleon propagator that ignores negative energy solutions of the free Dirac equation. Next, a Pauli reduction [6] is made to transform the current operator into a 2×2 matrix, and an expansion in powers of (q/M) and/or (p/M) (where M is the nucleon mass) is made [14]. Finally the transition nucleon current is calculated as the matrix element between bispinorial, nonrelativistic bound (ϕ_B) and scattered (ϕ_F) wave functions instead of the 4-component ψ_B, ψ_F wave functions. We then cast relativistic effects into:

i) *Kinematical*. These are effects due to the truncation of the current operator to first, or higher order in p/M , q/M . For moderate p/M values the relativized form proposed in [14] gives proper account of such effects.

ii) *Dynamical*. These are effects due to the differences between relativistic and nonrelativistic wave functions which depend not only on the 4-spinor versus 2-spinor structure, but also on the potentials used in the respective Dirac and Schrödinger equations for the bound and scattered nucleon. Salient features of dynamical effects are: a) A dynamical depression of the upper component of the scattered nucleon wave function in the nuclear interior, typically identified as the effect of the Darwin term coming from the derivative of the optical S-V potentials [6]. b) A dynamical enhancement of the lower components, mainly that of the bound nucleon wave function.

So far, we applied successfully RDWIA to ^{208}Pb and ^{40}Ca at low $|Q^2|$ [5,6], and to ^{16}O at high $|Q^2|$ [8,15]. The effect caused by the nonlocal Darwin term for ^{40}Ca and ^{208}Pb cases was studied in detail in refs. [5,6]. The Darwin term causes an apparent enhanced absorption when comparing the RDWIA differential cross-section to the DWIA one at moderate p_m values, thus predicting larger spectroscopic factors [5,6,16]. For larger missing momentum values ($p_m/(Mc) \geq 1/3$) the lower components of the relativistic wave functions start to play a more important role, enhancing the higher momentum components of the nucleon wave functions. In previous work [7] we found that RDWIA calculations, compared to standard DWIA, tend to produce lower cross sections at $p_m \leq 300$ MeV/c and larger cross-sections at $p_m \geq 300$ MeV/c, improving agreement [5–7] with experiment.

The effect of the dynamical enhancement of the lower components was studied in RPWIA in refs. [17,18]. It was also studied in RDWIA in ref. [8] at high $|Q^2|$. In both cases it was found to play a crucial role in the TL responses. Recent data [15] on ^{16}O at high $|Q^2|$ seem to confirm former RDWIA predictions. In particular, the richness shown by the structure of the A_{TL} asymmetry, which is different for $p_{1/2}$ and $p_{3/2}$ shells, is only consistent with predictions of relativistic calculations that include the dynamical enhancement of the lower components of bound Dirac spinors. Moreover, recent data on polarization observables in ^{12}C at $|Q^2| \approx 0.5$ (GeV/c) 2 also agree nicely with RDWIA analysis [19,20].

For ^{16}O there is an important controversy in the comparison of theory to data at low $|Q^2|$. We refer to the data sets from $1p$ -shell proton knockout experiments on ^{16}O performed at Saclay [21] and NIKHEF [22,23] in various kinematics in late 80's/early 90's. These experiments measured the cross-section as a function of missing momentum and, in particular Chinitz *et al.* [21] and Spaltro *et al.* [22], extracted also the TL response and A_{TL} asymmetry at $|Q^2| = 0.3$ (GeV/c) 2 and 0.2 (GeV/c) 2 , respectively. The measurements from Chinitz *et al.* were compared to relativistic [21] and nonrelativistic [22] DWIA calculations showing relatively small deviations from theory. On the other hand, the data of Spaltro *et al.* [22] were compared to results from standard nonrelativistic DWIA calculations, and were found to be far from theory. Using nonrelativistic optical potential parameters by Schwandt *et al.* [24], and spectroscopic factors fitted to data in parallel kinematics, Spaltro *et al.* [22] found that the experimental R^{TL} is enhanced by a factor $\simeq 2.05$ for the $1p_{3/2}$ shell and by a factor $\simeq 1.5$ for the $1p_{1/2}$.

Though the large discrepancy between DWIA results and experiment found by Spaltro *et al.* may in part be due to two-body currents, calculations of exchange current effects are still contradictory [25,26]. Hence, the controversy surrounding the TL response and asymmetry

data still persists. In view of forthcoming information on ^{16}O responses from experiments at Jefferson Lab in the near future, it is important to reexamine these sets of data with RDWIA calculations. We investigate whether a systematic fully relativistic analysis of the $(e, e'p)$ data at low $|Q^2|$ may explain the apparent discrepancies between data from Saclay [21] and NIKHEF [22,23].

The paper is organized as follows: in Section II we summarize the basic formalism needed to describe coincidence electron scattering reactions, paying special attention to the relativistic distorted wave impulse approximation (RDWIA). Section III contains the theoretical results obtained and their comparison with the experimental data. In section IV we present our conclusions.

II. DESCRIPTION OF $(E, E'P)$ CALCULATIONS

The general formalism for exclusive electron scattering reactions has been presented in detail in several previous papers. We refer in particular to refs. [1,5,27]. Here we just summarize the kinematics and focus on those aspects that are of relevance to the points under discussion in this paper. As a guide to the reader we write down the unpolarized cross-section in Born approximation assuming plane waves for the incoming and outgoing electron (treated in the extreme relativistic limit),

$$\frac{d\sigma}{d\Omega_e d\varepsilon' d\Omega_F} = K \sigma_{Mott} f_{rec} \left[v_L R^L + v_T R^T + v_{TL} R^{TL} \cos \phi_F + v_{TT} R^{TT} \cos 2\phi_F \right], \quad (2)$$

where ε' and Ω_e are the energy and solid angle corresponding to the scattered electron and $\Omega_F = (\theta_F, \phi_F)$ is the solid angle for the outgoing proton. The factor K is given by $K = |\vec{p}_F| E_F / (2\pi)^3$, with \vec{p}_F the momentum carried by the ejected proton and E_F its energy. The term f_{rec} is the usual recoil factor $f_{rec}^{-1} = |1 - (E_F/E_{A-1})(\vec{p}_{A-1} \cdot \vec{p}_F)/|\vec{p}_F|^2|$, where \vec{p}_{A-1} and E_{A-1} are the momentum and energy of the residual nucleus, respectively. The kinematical factors are $v_L = \lambda^2$, $v_T = \lambda/2 + \tan^2 \theta_e/2$, $v_{TT} = \lambda/2$, $v_{TL} = \lambda \sqrt{\lambda + \tan^2 \theta_e/2}$ with $\lambda = 1 - (\omega/|\vec{q}|)^2$, where ω and \vec{q} are the energy and momentum transfer in the reaction and θ_e the electron scattering angle. The above factors, that contain the dependence on the electron kinematics, coincide with those given in [27,28] except for a factor $\sqrt{2}$ in the interference TL term. We remark that in refs. [21,22] a different convention for K was used (see for instance eq. (1) of ref. [22]), which amounts to a factor M/E_F of the responses presented in this work with respect to the ones displayed in [21,22].

Our calculation of differential cross-sections and responses includes also the effect of Coulomb distortion of the incoming and outgoing electron waves. This breaks the simplicity of eq. (2), which is however still useful as a guide. Nevertheless, for ^{16}O Coulomb distortion effects in the electron wave functions are tiny (less than 1.5% effect on the cross-section).

The hadronic current enters only in the response functions R^α , $\alpha = L, T, TL, TT$ where L and T denote the longitudinal and transverse projections of the nuclear current with respect to the momentum transfer \vec{q} , respectively. Note that the response functions can be separated by performing measurements with different kinematical factors v_α and/or values of the azimuthal angle ϕ_F , while keeping the momentum and energy transfer constant. The response R^{TL} is obtained from differential cross-sections at $\phi_F = 0^\circ$ and 180° , both in theory

and in experiment. Experimental data for the cross-section are often presented in terms of *reduced cross-sections* or *effective momentum distributions* $\rho(\vec{p}_m)$, obtained by integrating over a particular missing energy peak the differential cross-section divided by $K(2\pi)^3\sigma_{ep}$. Thus $\rho(\vec{p}_m)$ is defined by,

$$\rho(\vec{p}_m) = \int_{\Delta E_m} \left(\frac{d\sigma}{d\Omega_e d\varepsilon' d\Omega_F dE_F} / (K(2\pi)^3\sigma_{ep}) \right) dE_m. \quad (3)$$

The free electron-proton cross-section, σ_{ep} , is usually taken as σ_{CC1} of de Forest [29]. One must be aware that the cross-section given in eq. (2) has a strong dependence in the kinematical variables via K and σ_{ep} which is removed in the reduced cross-section. For instance, at the kinematics of the experiment of Chinitz *et al.* [21] ($T_F = 160$ MeV, $|Q^2| = 0.3$ (MeV/c)² and $\varepsilon_{beam} = 580$ MeV) a small variation of 5 MeV in T_F and ω (keeping E_m and p_m constant), may change the cross-section by as much as 7% and the reduced cross-section by less than 2%. In order to minimize kinematical dependences, it is safer to determine spectroscopic factors by scaling the theory to data on reduced cross sections rather than to data on cross-sections. This is so because experimentally, a folding and average of the cross-sections, responses and/or reduced cross-sections is performed over the experimental acceptance, and central values for the kinematical variables are quoted. Theoretical calculations are done for the quoted central values. Due to this, it is not unusual that spectroscopic factors may depend on whether one chooses to set the scale by comparing to reduced cross-sections or to differential cross-sections, or even to separate responses. In this work we first derive the spectroscopic factor (S_α) from the reduced cross-section data. Then we use this same factor to compare to data for the individual responses. In this way the analysis of R^{TL} and other responses is more consistent and meaningful.

Another quantity also obtained by the experimentalists and discussed in next section is the asymmetry A_{TL} given by

$$A_{TL} = \frac{\sigma(\phi_F = 180^\circ) - \sigma(\phi_F = 0^\circ)}{\sigma(\phi_F = 180^\circ) + \sigma(\phi_F = 0^\circ)}. \quad (4)$$

One can see from eq. (2) that this observable is closely related to R^{TL} , with the advantage that it is free from the scale factor ambiguity.

A. Relativistic Distorted Wave Impulse Approximation (RDWIA)

In RDWIA the process is described [5] in terms of the one-body nucleon current given in eq. (1). The relativistic bound nucleon wave function, ψ_B , is a four-spinor with well defined angular momentum quantum numbers κ, μ , corresponding to the shell under consideration. In coordinate space it is given by:

$$\psi_\kappa^\mu(\vec{r}) = \begin{pmatrix} g_\kappa(r)\phi_\kappa^\mu(\hat{r}) \\ if_\kappa(r)\phi_{-\kappa}^\mu(\hat{r}) \end{pmatrix}, \quad (5)$$

which is eigenstate of total angular momentum with eigenvalue $j = |\kappa| - 1/2$,

$$\phi_\kappa^\mu(\hat{r}) = \sum_{m,\sigma} \langle lm \frac{1}{2}\sigma | j\mu \rangle Y_{lm}(\hat{r}) \chi_\sigma^{\frac{1}{2}} \quad (6)$$

with $l = \kappa$ if $\kappa > 0$ and $l = -\kappa - 1$ if $\kappa < 0$. The functions f_κ, g_κ satisfy the usual coupled linear differential equations [5,30,31].

The wave function for the outgoing proton, ψ_F , is a scattering solution of the Dirac equation, which includes S-V global optical potentials. This wave function is obtained as a partial wave expansion in configuration space [5,6]:

$$\psi_F(\vec{r}) = 4\pi \sqrt{\frac{E_F + M}{2E_F V}} \sum_{\kappa, \mu, m} e^{-i\delta_\kappa^*} i^l \langle l m \frac{1}{2} \sigma_F | j \mu \rangle Y_{lm}^*(\hat{P}_F) \psi_\kappa^\mu(\vec{r}), \quad (7)$$

where $\psi_\kappa^\mu(\vec{r})$ are four-spinors of the same form as that in eq. (5). The phase-shifts and radial functions are complex because of the complex potential.

The choice of the current operator \hat{J}^μ is to some extent arbitrary (see discussion in refs. [5,17,32]). Here we consider the two most popular choices denoted as CC1 and CC2 [29]:

$$\hat{J}_{CC1}^\mu = (F_1 + F_2)\gamma^\mu - \frac{F_2}{2M}(\bar{P} + P_F)^\mu \quad (8)$$

$$\hat{J}_{CC2}^\mu = F_1\gamma^\mu + i\frac{F_2}{2M}\sigma^{\mu\nu}Q_\nu, \quad (9)$$

where F_1 and F_2 are the nucleon form factors related in the usual way [33] to the electric and magnetic Sachs form factors of the dipole form. The variable \bar{P} in eq. (8) is the four-momentum of the initial nucleon for on-shell kinematics, *i.e.*, $\bar{P}^\mu = (E(p), \vec{p})$ ($E(p) = \sqrt{\vec{p}^2 + M^2}$ and $\vec{p} = \vec{p}_F - \vec{q}$).

Thus the evaluation of the one-body current matrix element involves the use of 4×4 -operators and 4-spinors with negative energy components. This is at variance with the nonrelativistic (DWIA) approximation where a truncated current operator is used [34] and matrix elements are evaluated between bispinorial wave functions (ϕ_B, ϕ_F). Therefore in the discussion of results in next sections we shall refer to relativistic kinematical effects –that have to do with the differences due to the use of the complete relativistic current operator instead of the truncated one– and to relativistic dynamical effects. A way to fully incorporate the kinematical relativistic effects was suggested in ref. [6,14], and studied in detail in ref. [35] for the reaction ${}^2H(e, e'p)$.

B. Remarks on relativistic dynamical effects

As mentioned in the introduction the dynamical effects come from the differences between relativistic and nonrelativistic potentials and wave functions. In ref. [6] we discussed in detail effects on reduced cross-sections for ${}^{208}\text{Pb}$ in parallel kinematics due to differences between the upper components of the four-spinors ψ_B, ψ_F which are Dirac solutions with S-V potentials and the bispinors ϕ_B, ϕ_F which are Schrödinger solutions with standard (Wood-Saxon type) potentials for bound and scattered nucleons.

To illustrate the meaning of this effect we recall that the Dirac equation with S-V potentials

$$(\tilde{E}\gamma_0 - \vec{p} \cdot \vec{\gamma} - \tilde{M})\psi = 0 \quad (10)$$

with

$$\tilde{E} = E - V(r) \quad (11)$$

$$\tilde{M} = M - S(r) \quad (12)$$

$$\psi = \begin{pmatrix} \psi_{up} \\ \psi_{down} \end{pmatrix}, \quad (13)$$

can be written either as a system of coupled linear differential equations for ψ_{up} , ψ_{down} , or as a second order differential Schrödinger like-equation for ψ_{up} containing also a first order derivative term (the Darwin term). Furthermore, using the transformation

$$\psi_{up}(r) = K(r)\phi(r), \quad (14)$$

the non-local (Darwin) term can be eliminated to obtain a more standard Schrödinger equation with second derivatives only

$$\left[\frac{-\vec{\nabla}^2}{2M} - U_{DEB} \right] \phi(\vec{r}) = \frac{(E^2 - M^2)}{2M} \phi(\vec{r}) \quad (15)$$

with U_{DEB} the Dirac equivalent potential [6] with central and spin-orbit terms

$$\begin{aligned} U_{DEB} &= V_C + V_{SO} \vec{\sigma} \cdot \vec{\ell} \\ V_C &= \frac{1}{2M} [V^2 - 2EV - S^2 + 2MS + V_D] \\ V_D &= \frac{1}{rA} \frac{\partial A}{\partial r} + \frac{1}{2A} \frac{\partial^2 A}{\partial r^2} - \frac{3}{4A^2} \left(\frac{\partial A}{\partial r} \right)^2 \\ V_{SO} &= \frac{1}{2M} \frac{1}{rA} \frac{\partial A}{\partial r} \\ A(r) &= \frac{\tilde{E} + \tilde{M}}{E + M} = K^2(r). \end{aligned} \quad (16)$$

The factor $K(r)$ relating the upper component of the Dirac solution (ψ_{up}) to the solution of the equivalent Schrödinger equation ($\phi(r)$) is called the Darwin factor. As it will be shown in next section, $K(r)$ produces a depletion of the outgoing wave function in the nuclear interior [36,37].

Another dynamical relativistic effect is that coming from the non-zero overlap with Dirac sea of the Dirac solutions with S-V potentials. The ψ_B , ψ_F wave functions have the general structure

$$\psi(\vec{p}) = \psi^{(+)}(\vec{p}) + \psi^{(-)}(\vec{p}), \quad (17)$$

where $\psi^{(+)}$ and $\psi^{(-)}$ are the projections on the positive and negative energy solutions of the Dirac equation for free particles:

$$\psi^{(+)}(\vec{p}) = \sum_s u_s(\vec{p}) \bar{u}_s(\vec{p}) \psi(\vec{p}) = \Lambda_{(+)}(\vec{p}) \psi(\vec{p}) \quad (18)$$

$$\psi^{(-)}(\vec{p}) = - \sum_s v_s(\vec{p}) \bar{v}_s(\vec{p}) \psi(\vec{p}) = \Lambda_{(-)}(\vec{p}) \psi(\vec{p}), \quad (19)$$

where we use the notation and conventions of Bjorken and Drell [33], so that the positive and negative energy projectors are

$$\Lambda_{(\pm)}(\vec{p}) = \frac{M \pm \overline{P}}{2M} \quad (20)$$

with $\overline{P}_\mu = (\overline{E}, \vec{p})$ and $\overline{E} = \sqrt{p^2 + M^2}$.

The positive and negative energy components of ψ can also be written as

$$\psi^{(+)}(\vec{p}) = \begin{pmatrix} \psi_{up}^{(+)}(\vec{p}) \\ \psi_{down}^{(+)}(\vec{p}) \end{pmatrix} = \sum_s \tilde{\alpha}(\vec{p}, s) u_s(\vec{p}) \quad (21)$$

$$\psi^{(-)}(\vec{p}) = \begin{pmatrix} \psi_{up}^{(-)}(\vec{p}) \\ \psi_{down}^{(-)}(\vec{p}) \end{pmatrix} = \sum_s \tilde{\beta}(\vec{p}, s) v_s(\vec{p}) . \quad (22)$$

Eqs. (21,22) make it more transparent what are the new ingredients of the relativistic calculation. In particular the difference between ψ_{down} and $\psi_{down}^{(+)}$ is what we call the dynamical enhancement of the down component. Explicit expressions and figures showing $\tilde{\alpha}(p)$ and $\tilde{\beta}(p)$ for several orbitals can be found in ref. [18]. Here we just mention that the dynamical enhancement of the down component is proportional to the nonzero Dirac sea overlap, $\tilde{\beta}(p)$, and that though it is small, it was found to play an important role in the TL response function in the RPWIA calculations presented in ref. [18], and in the RDWIA calculations at high $|Q^2|$ reported in refs. [8,15]. Its role for the present RDWIA calculations is discussed in next section. A way to define an effective 2×2 current operator that includes these dynamical relativistic effects was introduced in ref. [38].

C. Projected calculation

The sensitivity of the different scattering observables to the negative energy components can be analyzed by constructing properly normalized 4-spinors of the form in eq. (18). Then, one can compare the results obtained using the fully relativistic amplitude given in eq. (1) with those obtained when the negative energy components are projected out. This is done when the nucleon current is calculated as

$$J_{(++)}^\mu(\omega, \vec{q}) = \int d\vec{p} \overline{\psi}_F^{(+)}(\vec{p} + \vec{q}) \hat{J}^\mu(\omega, \vec{q}) \psi_B^{(+)}(\vec{p}) , \quad (23)$$

where $\psi_B^{(+)}$ ($\psi_F^{(+)}$) is the positive-energy projection of ψ_B (ψ_F), *i.e.*,

$$\psi_B^{(+)}(\vec{p}) = \Lambda_{(+)}(\vec{p}) \psi_B(\vec{p}), \quad \psi_F^{(+)}(\vec{p} + \vec{q}) = \Lambda_{(+)}(\vec{p} + \vec{q}) \psi_F(\vec{p} + \vec{q}) . \quad (24)$$

The dynamical enhancement of the lower components is contained in the current of eq. (1), but not in eq. (23). It is important to realize that the positive-energy projectors inserted in eq. (23) depend on the integration variable \vec{p} . One could also neglect this \vec{p} -dependence by using projection operators corresponding to asymptotic values of the momenta, *i.e.*, projectors acting on ψ_F and ψ_B respectively, with $P_F^\mu = (E_F, \vec{p}_F)$, $P_B^\mu = P_F^\mu - \overline{Q}^\mu$ the asymptotic four-momentum of the outgoing and bound nucleon respectively, with $\overline{Q}^\mu = (\overline{\omega}, \vec{q})$ and $\overline{\omega} = E_F - \sqrt{(\vec{p}_F - \vec{q})^2 + M^2}$. We refer to this approach

as *asymptotic projection*. This latter projection is almost equivalent to “EMA-noSV” procedure employed in ref. [39], in which the 4-spinors used have upper components identical to the upper components of the Dirac equation solutions, but the lower components are obtained with an additional approximation, the effective momentum approach (EMA). Although EMA-noSV approach also neglects the enhancement of the lower components, it is not at all equivalent to the exact projection method in eqs. (23,24). The EMA-noSV approach computes the nucleon current with four-spinors that have the same structure than the ones encountered in the scattering of free nucleons, because it enforces the relationship between upper and lower components to be driven by the asymptotic value of the momenta at the nucleon vertex. In particular, the Gordon transformation is exact for EMA-noSV approach. Therefore, CC1 and CC2 operators would lead to identical results within EMA-noSV, provided the same choices for the off-shell values of ω , E , E_F , \vec{p} and \vec{p}_F are made. This would be a strong prerequisite to a factorized calculation, though still not a sufficient condition. In order to keep the drawings in section III clear enough, we do not show in the figures the results obtained within EMA-noSV, but we shall comment how this approach compares with the fully relativistic and/or the projected one.

III. RESULTS AND DISCUSSION

In this work we consider three data sets for nucleon knockout from $p_{1/2}$ and $p_{3/2}$ shells in ^{16}O that correspond to kinematical conditions of three different experiments. We summarize them as follows:

Set (a) corresponds to the experiment of Leuschner *et al.* at the Medium Energy Accelerator (MEA) at NIKHEF-K [23]. The coincidence reaction $^{16}\text{O}(e, e'p)^{15}\text{N}$ was analyzed in quasielastic parallel kinematics at three different beam energies: 304, 456 and 521 MeV. The total kinetic energy of the outgoing proton was around 90 MeV. The spectral function of ^{16}O was measured in the range, $0 < E_m < 40$ MeV and $-180 < p_m < 270$ MeV/c, where E_m and p_m are the missing energy and missing momentum, respectively.

Set (b) corresponds to the experiment performed at the Saclay Linear Accelerator by Chinitz *et al.* [21]. The kinematical setup was constant $|\vec{q}| - \omega$ kinematics. The electron beam energy was $\varepsilon = 580$ MeV, the outgoing proton kinetic energy $T_F = 160$ MeV, and the transfer momentum and energy: $|\vec{q}| = 570$ MeV/c and $\omega = 170$ MeV ($|Q^2| = 0.3$ (GeV/c) 2). The missing energy resolution was 1.3 MeV, which made not possible to resolve the $(5/2^+, 1/2^+)$ doublet at an excitation energy $E_x = 5.3$ MeV in ^{15}N from the $3/2^-$ state at $E_x = 6.3$ MeV.

Set (c), also in $|\vec{q}| - \omega$ constant kinematics, was obtained by Spaltro *et al.* [22] with the two high-resolution magnetic spectrometers at the medium-energy electron accelerator MEA of NIKHEF-K. Data were measured at momentum and energy-transfer values centered at $(\omega, |\vec{q}|) = (90 \text{ MeV}, 460 \text{ MeV/c})$, *i.e.*, close to the center of the quasielastic peak at $|Q^2| \simeq 0.2$ (GeV/c) 2 . The experiment covered a missing momentum range from 30 to 190 MeV/c. The missing energy resolution was about 180 keV, which made it possible to resolve the $(5/2^+, 1/2^+)$ doublet from the $3/2^-$ state.

Next we discuss our results for spectroscopic factors, reduced cross-sections and responses corresponding to these sets of data and kinematical conditions.

In subsection III.A we deduce spectroscopic factors from reduced cross sections, that are then used in subsection III.B for response functions. Subsection III.A discusses also results corresponding to different relativistic S-V potentials. In our previous work on ^{40}Ca and ^{208}Pb we found that spectroscopic factors were larger than the ones obtained with the nonrelativistic analyses and were very stable when different parameterizations of the S-V potentials for bound (HS, NLSH) [5,7] and scattered (EDAI, EDAD1, EDAD2, EDAD3) [6] protons were used. We shall see that the case of ^{16}O that we examine here is different in several respects.

A. Reduced Cross Section and Spectroscopic Factors

Let us first discuss the comparison of theory and experiment on reduced cross-sections for set (a) (Leuschner *et al.* [23]). We recall that because of parallel kinematics, for this set the only response functions that contribute to the cross-sections are R^L and R^T . Fig. 1 shows the reduced cross-section for $p_{1/2}$ and $p_{3/2}$ shells. The sign of p_m refers to the projection of the initial nucleon momentum along the direction of the transfer momentum \vec{q} . It is defined to be positive for $|\vec{q}| < |\vec{p}_F|$ and negative for $|\vec{q}| > |\vec{p}_F|$. Fully relativistic calculations using the CC1 and CC2 current operators (RCC1, RCC2) are shown by thin and thick lines respectively. Throughout this paper we use the Coulomb gauge. The Landau gauge produces similar results. Gauge ambiguities [40] are rather small for the fully relativistic results in these two gauges [17,18].

Spectroscopic factors for each of the two shells are evaluated by scaling theoretical calculations to experimental data. They are listed in Table I for different choices of wave functions and current operators. In this table we also quote the statistical error within parenthesis and the χ^2 values per degree of freedom.

Results on the right panel in Fig. 1 correspond to bound state wave function calculated using the parameters of the set NLSH [41]. Results with the older HS set [12,31], as well as with the newest NL3 one [42] are similar. For the scattered proton wave function we use the energy-dependent A -independent potential derived by Clark *et al.* [13] for ^{16}O (EDAI-O). Two things are striking in these results that are at variance with the situation we met in previous works on ^{40}Ca and ^{208}Pb [5,6]:

1. There are clear deviations in the shape of theoretical and experimental effective momentum distributions in the right hand side panel of Fig. 1. Actually, the NLSH wave functions have smaller (larger) r.m.s. radii in r-space (p-space) than what is shown experimentally.
2. The spectroscopic factors are small, of the same order or even smaller than nonrelativistic ones when Perey factor is included in the latter. As seen in Table I the spectroscopic factors increase when global A -dependent type (EDAD-1,-2) potentials are used instead of the A -independent potential fitted to ^{16}O (EDAI-O). Moreover, the χ^2 values are large for NLSH bound wave functions independently of the optical potential used.

We have verified that all EDAD-type calculations (EDAD-1,-2,-3) give similar results on reduced cross-sections and responses. Compared to EDAI-O they give about 15 – 20%

smaller reduced cross-sections with almost identical shapes. Consequently, EDAD-1,-2,-3 spectroscopic factors are 15 – 20% larger than EDAl-O ones but the χ^2 values are analogous (see Table I). Why this is different from the cases we analyzed in refs. [5,6] can be easily understood from Fig. 2. In this figure we compare the relativistic central potentials (S, V) and Darwin factors (K) corresponding to EDAl-O and to EDAD-1,-2 optical potentials for ^{208}Pb (right panels) and for ^{16}O (left panels). We can see that in the case of ^{16}O , EDAD-1,-2 potentials produce a deeper $K(r)$, *i.e.*, a larger reduction of the scattered wave in the nuclear interior than EDAl-O potential –also, V_C is somewhat more absorptive–, while in the case of ^{208}Pb both are about the same. Consequently, at the energies considered, EDAD-1,-2 potential lead to larger spectroscopic factors than EDAl-O in ^{16}O , while the two potentials lead to similar spectroscopic factors in ^{208}Pb . The same is true for EDAD-3 and other versions of the relativistic EDAD potentials.

To have a more conclusive determination of ^{16}O spectroscopic factors one would need to constrain the optical potential choice by means of inelastic (p, p') data, in addition to the elastic ones [43]. But this is not available for the small knock-out proton energies (~ 90 MeV) considered here nor in a fully relativistic framework.

The large χ^2 values in the left part of Table I for all the optical potentials have to do with the fact that the data do not follow the shape of theoretical reduced cross-sections in the right panel of Fig. 1. A similar problem has been found for data sets (b) and (c) where the quality of NLSH fits is even worse. This, after all, is not surprising because the standard Lagrangians, like NLSH, are fitted to bulk properties of a few heavy nuclei, and one may expect that the predicted r.m.s. radii of ^{16}O orbitals differ somewhat from experiment. Unfortunately, as seen in Table I this produces large uncertainties in spectroscopic factors. To solve this problem we may adjust the parameters of the relativistic potentials (or Lagrangian) so as to obtain the correct values of the single particle energies and r.m.s. radii for the orbitals considered, in an analogous way to what is usually done in nonrelativistic analyses of ($e, e'p$) data. This is what we do next.

Compared to data sets (b) and (c), data set (a) has many more data points extending over a larger p_m range. Therefore, this data set can be used much more reliably to determine *simultaneously* spectroscopic factors and r.m.s.r. values. We have then adopted the following strategy: First, we use data set (a) to slightly tune the parameters of the NLSH potential so as to reproduce the experimental binding energies and r.m.s.r. values of the $p_{1/2}$ and $p_{3/2}$ orbitals in ^{16}O , closely resembling the standard nonrelativistic procedure. We denote by NLSH-P the new relativistic potentials and wave functions (see Table II). These new relativistic wave functions are then used to make predictions for the kinematical conditions of data sets (b) and (c).

The NLSH-P wave functions are obtained by changing the parameters of the NLSH Lagrangian so that the radii and depth of the S and V potential wells derived from the Lagrangian are modified in the same proportion. The negative energy content of the resulting bound state wave function is barely changed by this procedure. The rescaling of the depth size and radii of the NLSH-P wells is within 10% of the initial NLSH ones. The improvement obtained in the description of the shapes and quality of the fits is clearly visible in Fig. 1 and Table I.

The role played by relativistic dynamical effects is also analyzed from the results presented in Fig. 1 and Table I. Each curve in Fig. 1 is scaled by the corresponding spectro-

scopic factors in Table I. The reduced cross-sections evaluated after projecting the bound and scattered proton wave functions over positive energy states (see eq. (23)) are shown by thin-dashed (PCC1) and thick-dashed (PCC2) lines. Note that the difference between PCC1 and PCC2 results is very small because the so-called Gordon ambiguities are reduced after projection [17,18]. The results obtained using the asymptotic values of the momenta in the projection operator as described in section II.B, are almost identical to the PCC2 results and thus are not shown here. Once the global scale factor is taken into account, all the calculations predict a very similar behavior, what indicates that, aside from the Darwin term, the effect of relativistic dynamics in the reduced cross-sections is not important in parallel kinematics at low values of $|Q^2|$. This agrees with a recent work by Giusti and collaborators [4]. This observation also agrees with results of some previous works [8,17,18] where we saw that the dynamical enhancement of the lower component makes an important effect in the cross-section mainly at high missing momentum values and/or in the R^{TL} response function (which *does not contribute in parallel kinematics*), whereas its influence on R^L and R^T is quite modest.

Comparing the fully relativistic results with NLSH-P wave functions for CC1 and CC2, one observes that the differences are at most of the order of $\sim 8\%$. In the case of the projected calculation, we note that the spectroscopic factors are slightly larger than those corresponding to a fully relativistic calculation. This is due to the enhancement of the lower components of the wave functions which is not contained in the projected approximations. Their effect is negligible for CC2 operator and is enhanced by the CC1 choice. We recall that another dynamical relativistic effect, namely the Darwin term, is contained in all the figures and tables shown here. For EDAI-O optical potential this effect amounts to a 10% reduction of the reduced cross-section in ^{16}O for the kinematics discussed in this work. This is comparable to the effect of the Perey factor that was included in nonrelativistic DWEEPY calculations [22,23] while for EDAD-optical potentials this amounts to a 20% reduction.

One thus expects the spectroscopic factors listed in Table I for EDAI-O in the projected case to be similar to those obtained from fits with standard nonrelativistic DWIA calculations including Perey factors. In this last case the extracted factors for various choices of optical potentials are $0.60 \leq S_\alpha \leq 0.65$ for $p_{1/2}$, and $0.49 \leq S_\alpha \leq 0.60$ for $p_{3/2}$ [23], which are also roughly in agreement with those in Table I for NLSH-P and EDAD-type potentials.

A smaller spectroscopic factor is expected for the $p_{3/2}$ shell than for the $p_{1/2}$, because the $p_{3/2}$ strength is known to be fragmented into three states: the state considered here at $E_m = 18.4$ MeV, and two weaker peaks at around 22.0 and 22.7 MeV. According to [23,44] the two higher lying peaks would contain about 10% of the total $p_{3/2}$ strength. The spectroscopic factors determined from data set (a) indicate that, taking this extra 10% contribution into account, there is similar $3/2^-$ and $1/2^-$ spectroscopic strength.

In what follows we use the new bound state wave functions (NLSH-P) to make predictions for comparison to the other data sets (b) and (c). We stress that we have used high quality data to fix the size of the wave function and that because data set (a) corresponds to parallel kinematics no experimental information on the R^{TL} response has been employed.

Let us now focus on the spectroscopic factors obtained from reduced cross-sections in data sets (b) and (c). Fig. 3 shows the reduced cross-sections for $p_{1/2}$ and $p_{3/2}$ shells. Left and right panel correspond respectively to data sets (b) and (c). As in Fig. 1, for each curve a global scale factor has been fitted to the experimental data. The corresponding scale

factors and their statistical errors are listed in Table III. Similarly to what we saw for set (a), also for sets (b) and (c) EDAD-type optical potentials give larger spectroscopic factors than EDAl-O (see also Fig. 4).

The results for the $p_{3/2}$ shell corresponding to the Saclay experiment (left panel) include the contribution of the $(5/2^+, 1/2^+)$ doublet. We have verified that the change in the shape of the responses or reduced cross-section after inclusion of the doublet is small. The main effect of its inclusion is a decrease of the deduced spectroscopic factor for the $p_{3/2}$ shell of the order of 10%. In ref. [21] the contribution of this doublet was subtracted from the experimental data with a procedure based on a nonrelativistic formalism. We have chosen to use the uncorrected data from ref. [44], and include the contribution from the doublet in our theoretical calculation. The $s - d$ content has been determined through fits to data set (a) for this state [23]. The values of the spectroscopic factors are $S_{1/2^+} = 0.034(2)$ (RCC1), $0.034(2)$ (RCC2), $S_{5/2^+} = 0.086(5)$ (RCC1), $0.088(5)$ (RCC2) (with a χ^2/dof of the order of 0.5).

Let us now discuss the results corresponding to data set (b) in left panel of Fig. 3. As shown, the calculations reproduce in general the experimental data for both shells with the scale factors listed in Table III. Although the various approximations give similar results, we note that the RCC1 (thin solid line) reduced cross-sections for the $p_{1/2}$ shell are less symmetrical around $p_m = 0$, a behavior that is not favored by the data. For this data set (b) all the calculations, except RCC1 for the $p_{1/2}$ shell, reproduce well the asymmetry of the reduced cross-section. We will return to this point when talking about the TL observables in next section. Finally, it is important to remark that the spectroscopic factors obtained from the data set (b) (Table III) agree, within statistical errors, with those obtained from data set (a) taking into account the systematic error of both experiments: around 5.4% for data set (a) [23] and 6.3% for data set (b) [44].

Concerning set (c) [22] the data on reduced cross-sections in right panel of Fig. 3 have been obtained from the differential cross-sections and detailed kinematics setup in Appendices A and D of ref. [45] (the systematic error for data set (c) reduced cross-section is 6% [22]). For the $p_{1/2}$ shell, the reduced cross-section is well reproduced by both relativistic and projected calculations, except in the case of the RCC1 calculation (thin solid line) that underestimates the data for negative missing momentum values. This is consistent with the results previously discussed for data set (b). For this shell, the spectroscopic factors that fit data set (c) are larger than the ones derived from data sets (a) or (b), but they are all compatible within statistical errors. In the case of the $p_{3/2}$ shell, although the shape of the cross-section is well reproduced by the various calculations, the situation on the spectroscopic factors is clearly different (see Table III). With EDAl-O optical potential the values of the spectroscopic factors that fit the $p_{3/2}$ data on reduced cross-sections in set (c) are 25 – 30% larger than the ones obtained from data set (a). These scale factors are also larger than the ones obtained from data set (b), but in this case the discrepancy is of the order of 15%, which is comparable to the combined systematic and statistical error for these values. EDAD-type potentials not only give larger spectroscopic factors but also give, on average, better agreement between $p_{3/2}$ spectroscopic factors of the three different sets (a), (b) and (c). This is seen in detail in Tables I and III and is further illustrated in Fig. 4.

In summary, the shapes of the reduced cross-sections are well described by all the RCC2 calculations and data sets, what makes us conclude that we can rely on the spectroscopic

factors derived with EDAD-1 and NLSH-P potentials. Thus the differences in the $p_{3/2}$ spectroscopic factors (see Fig. 4) obtained with the same ingredients (wave functions, operators and optical potentials) may be attributed either to a global scale variation among the three experiments for the $p_{3/2}$ shell, or to limitations of the theory. Coupled channel contributions or MEC could possibly make a different effect for the three kinematics analyzed in this work.

B. Response Functions and longitudinal-transverse Asymmetry

In this section we present results for the response functions and asymmetries and compare them to the data in sets (b) and (c) measured at Saclay [21] and NIKHEF [22], respectively. As already mentioned, these two experiments were performed under $|\vec{q}| - \omega$ constant kinematics so that the TL response and asymmetry (R^{TL}, A_{TL}) can be obtained from the cross-sections measured at $\phi_F = 0^\circ$ and $\phi_F = 180^\circ$ with the other variables (ω, Q^2, E_m, p_m) held constant. Moreover, the response functions $R^L + \frac{q^2}{2Q^2}R^{TT}$ and R^T were also determined for data set (c) [22].

Figs. 5 and 6 show respectively R^{TL} and A_{TL} for $p_{1/2}$ (upper panels) and $p_{3/2}$ (lower panels) corresponding to set (b) (left panels) and set (c) (right panels). In each panel we present four curves with the same conventions as in previous figures: RCC1 (thin solid), RCC2 (thick solid), PCC1 (thin-dashed) and PCC2 (thick-dashed). Each R^{TL} curve is scaled with the corresponding spectroscopic factor quoted in Table III. As it was also the case for reduced cross-sections, there are no appreciable differences in the shapes of curves obtained with the different types of optical potentials. Obviously, the asymmetry A_{TL} is independent on the value of the spectroscopic factor. The results for the $p_{3/2}$ shell in bottom-left panel of Figs. 5 and 6 include the contribution of the $(5/2^+, 1/2^+)$ doublet as explained for set (b) in previous section. The asymmetry A_{TL} was not produced by the Saclay experiment (set(b)), but we have deduced A_{TL} from the data using the R^{TL} values as well as the cross-section data in [44].

In Fig. 5 we also show by dotted lines the nonrelativistic results of ref. [22]. For comparison to previous studies in refs. [21,22], we quote in Table IV the factor required to scale the theoretical predictions to the R^{TL} data, additional to the factors in Table III. A value of one in this table indicates that the same spectroscopic factor fits *both* the reduced cross-section and R^{TL} , *i.e.*, indicates that the TL strength is consistently predicted by the theory.

Let us first discuss the comparison between theory and experiment for data set (b). From the results shown in Figs. 5 and 6, it is clear that the effects of the negative-energy components show up more in R^{TL} and A_{TL} than in the cross-sections (Fig. 3). In the case of the $p_{1/2}$ shell (left-top panel of Fig. 5), the RCC2 calculation agrees with experimental data within statistical errors, while PCC1 and PCC2 results for R^{TL} (dashed lines) lie about a 30-50% below the data, and the RCC1 calculation (thin solid line) overestimates the R^{TL} response by around 20% (see Table IV). In the case of the $p_{3/2}$ orbit (left-bottom panel), all the approximations predict similar curves: The projected results are much closer to fully relativistic ones than for the $p_{1/2}$ shell. Overall, the fully relativistic calculations seem to be favored by the data. The fact that in this shell the variation introduced by the negative energy components is much smaller than for the $p_{1/2}$ shell explains why the difference between RCC1 and RCC2 results is smaller for the $p_{3/2}$ than for the $p_{1/2}$ shell.

These results agree with the conclusion reached from RPWIA calculations in ref. [18] about the behavior of $j = \ell \pm 1/2$ spin-orbit partners which was also corroborated in RDWIA calculations at high $|Q^2|$ [8].

With regards to the TL observable, independent on the spectroscopic factor, we may conclude that for $p_{1/2}$ shell, A_{TL} is best reproduced by RCC2 results, while for $p_{3/2}$ shell the four theoretical results are very close together, and the experimental data agree with all of them.

In the right panels of Figs. 5 and 6 we see the results corresponding to data set (c). Most of the comments on data set (b) apply also here, though the data are somewhat more scattered and have larger error bars. In the case of the $p_{1/2}$ shell, PCC1 and PCC2 results are very similar and lie below the data; among the fully relativistic calculation, the RCC2 result reproduces the data within statistical errors, while RCC1 overestimates them by a 35%. In the case of the $p_{3/2}$ shell (bottom-right panel), all the calculations underestimate the experimental TL response by around 17-28%, except RCC1 for which the “additional” factor in Table IV is compatible with one within statistical errors.

In Fig. 7 we show the results for the responses $R^L + v_{TT}/v_L R^{TT}$ (top panels) and R^T (bottom panels) for the $p_{1/2}$ and $p_{3/2}$ shells compared to the data from NIKHEF [22]. Each curve is scaled with the spectroscopic factors quoted in Table III. Notice that these responses are rather insensitive to dynamical enhancement of lower components. This is consistent with the behavior observed in Fig. 1 and also with results of RPWIA calculations [18]. The results in Fig. 7 indicate that the separated responses are in general well reproduced by the relativistic as well as by the projected calculations for both shells, exception made of the data point at the lowest missing momenta where, as indicated by the large error bars, the L/T separation is more problematic.

Summarizing, for the $p_{1/2}$ shell the RCC2 results agree well with all observables and data sets, while RCC1 (projected) calculations show a too large (small) R^{TL} and A_{TL} . For the $p_{3/2}$ shell the theoretical calculations lie much closer together, and generally agree with all data sets and observables, except for R^{TL} and A_{TL} of data set (c). Although the R^{TL} , A_{TL} data on $p_{3/2}$ in set (c) lie higher than theoretical calculations, they are almost compatible with RCC1 and RCC2 calculations within statistical errors. This situation is quite different from the one found in ref. [22], which is also shown for comparison in Fig. 5. The dotted lines in this figure show the nonrelativistic results of ref. [22] that were obtained with nonrelativistic spectroscopic factors (0.61(3) for $p_{1/2}$ and 0.53(3) for $p_{3/2}$) and standard (Woods-Saxon type) nonrelativistic optical potentials and bound wave functions. The latter were also fitted to Leuschner data [23].

C. Further Discussion on TL observables

In this section we focus in Fig. 5 comparing our results to previous nonrelativistic ones. The dotted curves -representing the nonrelativistic calculations by Spaltro *et. al.* [22]- clearly underestimate TL responses for all shell and data sets. The deviation from data is larger for $p_{3/2}$ shell, particularly in data set (c), where the dotted curve gives roughly one half of the experimental TL response. Why is it that relativistic results in this figure are so much closer to data than nonrelativistic ones?.

We have examined in detail effects due to the various aspects that are relevant in comparing relativistic to nonrelativistic results. The effects of Darwin term are already taken into account as they basically affect the spectroscopic factors. The effects of the negative energy components, as already mentioned, are very small for R^L , R^T responses in all data sets (*a*), (*b*) and (*c*) but, as seen in Fig. 5 and Table IV, they are important for TL observables in data sets (*b*) and (*c*), particularly for the $p_{1/2}$ shell. We are then left to consider the effect of truncation of the current operator (TCO). TCO produces also a negligible effect at the kinematics of data set (*a*), but it is more important at the kinematics of data sets (*b*) and (*c*). This again affects more the TL responses and asymmetries where it may represent up to a 15% effect (see also ref. [4]). Thus for $p_{1/2}$ shell, TCO roughly explains the difference at the maxima between dotted curves and the curves obtained with projected calculations. However for $p_{3/2}$ shell TCO explains only a small fraction of the difference between dotted curves and results of projected calculations. The largest fraction of this difference is due to the use of a too small spectroscopic factor (see ref. [22]) that was taken from ref. [23] and that by no means fits the data on reduced cross-sections in set (*c*). As seen in Tables I, III and Fig. 4 the spectroscopic factor deduced from reduced cross-sections in data set (*c*) is 25 – 30% larger than that from data set (*a*).

The message from this is, not only that relativistic effects are important in perpendicular kinematics at low $|Q^2|$, but also that a careful analysis of all pieces of information has to be done to get a consistent picture of the three different sets of data. Since R^{TL} responses are known to be sensitive not only to relativistic effects but also to exchange currents, or other possible many-body effects, it is important to establish a clear framework that allows to look for the proper magnitude of such effects.

Indeed if we compare our results to data for the A_{TL} observable that is free from spectroscopic factor ambiguities, we find that all data are well reproduced with the standard CC2 current operator, except the $p_{3/2}$ data in set (*c*) which are only larger than theory by a factor ~ 1.17 . This is to be compared to the 2.05 factor that one could expect from ref. [22].

IV. SUMMARY AND CONCLUSIONS

In summary we find that the fully relativistic treatment improves substantially the description of reduced cross-sections and individual responses of all three sets of data on $^{16}\text{O}(e, e'p)$ at low $|Q^2|$. Although predictions from CC1 and CC2 current operators are rather close in most cases, data seem to favor the CC2 current operator. Therefore our remarks here will focus mainly on results with CC2 and with the improved NLSH-P bound nucleon wave functions, that have the correct r.m.s. radius. Using the most complete set of data on reduced cross-sections in parallel kinematics of Leuschner *et al.* [23] (set (*a*)) we obtain spectroscopic factors ranging from 0.58 to 0.64 for $p_{1/2}$ and from 0.45 to 0.55 for $p_{3/2}$, depending on whether we use A-independent (EDAI-O) or A-dependent (EDAD-1,2,3) optical potentials. In ^{16}O , the latter potentials produce a larger Darwin effect, thus larger spectroscopic factors. Compared to the cases studied in previous works on ^{40}Ca and ^{208}Pb , the determination of spectroscopic factors in ^{16}O with the relativistic approach is different in several respects. In the former cases, the standard NLSH wave functions were found to reproduce well the shapes of reduced cross-sections and the only fitted parameter was the spectroscopic factor. The latter was practically independent on the optical potential used

and was ~ 0.7 for the levels just below the Fermi level. On theoretical grounds smaller spectroscopic factors for ^{16}O are expected. In particular, from shell model Monte Carlo calculations on ^{16}O [46], one may expect $S_\alpha \sim 0.5$ though other theories predict somewhat larger values [47,48]. Larger spectroscopic factors are obtained from Spaltro *et al.* data [22] on reduced cross-sections in perpendicular kinematics (set (c)), while Chinitz's *et al.* data [21] also in perpendicular kinematics (set (b)) give similar spectroscopic factors than set (a). As one can see in Fig. 4, within error bars, spectroscopic factors derived from all data sets with EDAD-1 are compatible with each other. To overcome the uncertainty due to the optical potential (see also Fig. 4) one would need to fit the relativistic potential to both elastic and inelastic proton scattering data from ^{16}O in a manner similar to what has been done for nonrelativistic potentials [43]. The analyses of individual responses is practically independent on the optical potential, once they are scaled by the corresponding spectroscopic factors.

There is a long standing controversy surrounding the TL data for the $p_{1/2}$ and $p_{3/2}$ shells measured at Saclay [21] and NIKHEF [22]. We have therefore paid particular attention to TL responses and asymmetries and we conclude that there is not a fundamental inconsistency. Even at the low $|Q^2|$ values considered here, the TL response is much more sensitive than L and T responses to relativistic effects, in particular to the dynamical enhancement of the lower components. The role played by the latter is appreciated comparing fully relativistic results (RCC2 or RCC1) to those obtained using wave functions projected on the positive energy sector (PCC2 or PCC1). RCC2 results agree well with experimental TL responses on $p_{1/2}$ (as well as with TL asymmetries) which are underestimated by PCC2 and overestimated by RCC1, because CC1 current operator overemphasizes the role of negative energy components. The overall agreement with data on TL responses and asymmetries from set (b) and set (c) is quite satisfactory, with the exception of data on $p_{3/2}$ shell from set (c), but even in this case theory is much closer to experiment than previously found in ref. [22]. In particular, the large difference between data on TL responses from the two different sets is well accounted for by the present analyses. This is in contrast with the situation depicted in ref. [22], which is represented by dotted lines in Fig. 5.

In short, the puzzle of the large discrepancy in the TL-response obtained in Saclay [21] and NIKHEF [22], and the “additional” TL-strength found in both experiments is, to a large extent, explained by the effect of the negative energy components in the wave functions –a dynamical relativistic effect that may not have been expected at low transfer and missing momentum.

The large general mismatch of data set (c) on $p_{3/2}$ shell seems to point to a normalization problem which would require experimental verification. Our analyses indicate that the problem is not so much connected to the TL response, but rather to the normalization used. Nevertheless, since meson exchange currents and particularly isobar currents are claimed to affect more the $p_{3/2}$ than the $p_{1/2}$ orbitals [49], it would be interesting to see whether our fully relativistic calculation extended to include the isobar and other meson exchange effects would lead to better agreement with TL $p_{3/2}$ data from set (c). It will also be interesting to see how relativistic and nonrelativistic approaches compare to new data expected from future experiments that have been approved to measure reduced cross-sections and TL-responses in ^{16}O with unprecedented precision at Jefferson Lab.

This work was partially supported under Contracts No. PB/98-1111, PB/98-0676,

PB/96-0604 and by the Junta de Andalucía (Spain). J.R.V. and A.E. acknowledge support from doctoral fellowships of the Consejería de Educación de la Comunidad de Madrid and Ministerio de Educación y Cultura (Spain), respectively.

TABLES

		NLSH				NLSH-P			
		$p_{1/2}$		$p_{3/2}$		$p_{1/2}$		$p_{3/2}$	
		CC1	CC2	CC1	CC2	CC1	CC2	CC1	CC2
RELATIVISTIC									
EDAI-O	S_α	0.58(1)	0.64(2)	0.45(3)	0.49(3)	0.54(1)	0.58(1)	0.43(1)	0.45(1)
	χ^2/dof	6.6	4.5	25.3	15.7	1.3	1.3	2.7	3.5
EDAD-1	S_α	0.63(4)	0.72(2)	0.56(3)	0.62(2)	0.58(1)	0.64(1)	0.52(1)	0.55(2)
	χ^2/dof	9.6	3.7	15	7.2	1.2	1.2	1.2	4.8
EDAD-2	S_α	0.61(4)	0.69(3)	0.53(3)	0.59(2)	0.56(1)	0.62(1)	0.50(1)	0.52(1)
	χ^2/dof	10	2.6	18	9.2	1.4	1.1	1.7	4.1
PROJECTED									
EDAI-O	S_α	0.65(2)	0.66(2)	0.51(3)	0.52(3)	0.58(1)	0.59(1)	0.47(1)	0.46(1)
	χ^2/dof	4.5	3.2	16.9	13.3	1.2	1.6	3.6	4.3
EDAD-1	S_α	0.72(3)	0.74(2)	0.64(3)	0.64(2)	0.64(1)	0.65(2)	0.57(2)	0.56(2)
	χ^2/dof	4.0	2.6	7.6	5.9	1.4	1.6	4.4	6.3
EDAD-2	S_α	0.69(3)	0.71(2)	0.61(3)	0.61(3)	0.62(1)	0.63(1)	0.55(2)	0.54(2)
	χ^2/dof	4.6	3.1	9.7	7.4	1.3	1.5	3.7	5.3

TABLE I. Spectroscopic factors derived from Leuschner’s experimental reduced cross sections in ref. [23] (data set (a)) using NLSH and NLSH-P relativistic bound nucleon wave functions, and EDAI-O, EDAD-1 and EDAD-2 relativistic optical potential parameterizations (see text). Results with EDAD-3 are almost identical to the ones with EDAD-1. The numbers within parentheses indicate the statistical error.

	$p_{1/2}$			$p_{3/2}$		
	<i>b.e.</i> (MeV)	<i>r.m.s.r.-r</i> (fm)	<i>r.m.s.r.-p</i> (MeV)	<i>b.e.</i> (MeV)	<i>r.m.s.r.-r</i> (fm)	<i>r.m.s.r.-p</i> (MeV)
NLSH	11.4	2.838	175.7	18.8	2.679	185.2
NLSH-P	12.1	3.043	170.6	18.4	2.907	173.6

TABLE II. Comparison of binding energies and *r.m.s.r.* radius in *p*– and *r*– space for the wave functions NLSH [41] and NLSH-P. The contribution from the negative energy components to the norm of the wave function is about 2% in all cases.

	Set (b) Chinitz <i>et al.</i> [21]				Set (c) Spaltro <i>et al.</i> [22]			
	$p_{1/2}$		$p_{3/2}$		$p_{1/2}$		$p_{3/2}$	
	CC1	CC2	CC1	CC2	CC1	CC2	CC1	CC2
EDAI-O (R)	0.54(4)	0.56(3)	0.49(2)	0.51(2)	0.57(3)	0.61(2)	0.56(1)	0.59(2)
EDAI-O (P)	0.59(4)	0.56(4)	0.53(4)	0.53(3)	0.66(2)	0.63(2)	0.61(1)	0.61(2)
EDAD-1 (R)	0.59(4)	0.61(3)	0.53(3)	0.55(3)	0.68(4)	0.72(2)	0.62(2)	0.67(2)
EDAD-1 (P)	0.65(4)	0.62(3)	0.57(5)	0.57(4)	0.79(3)	0.74(3)	0.69(3)	0.69(3)

TABLE III. Spectroscopic factors derived from two different sets of data on experimental reduced cross sections from the full relativistic approach (R) and from the projected one (P). The nomenclature used is the same as in Table I. The numbers within parentheses show the statistical error only. All results correspond to the NLSH-P bound wave function.

	Set (b)				Set (c)			
	$p_{1/2}$		$p_{3/2}$		$p_{1/2}$		$p_{3/2}$	
	N_{TL}	χ^2/dof	N_{TL}	χ^2/dof	N_{TL}	χ^2/dof	N_{TL}	χ^2/dof
RCC1	0.83(10)	0.65	0.95(17)	5.3	0.63(10)	1.1	1.09(12)	3.2
PCC1	1.32(42)	4.5	1.14(22)	5.8	1.15(17)	1.1	1.28(12)	2.5
RCC2	1.14(12)	0.49	1.02(15)	3.4	0.90(13)	1.0	1.17(12)	2.5
PCC2	1.48(32)	2.2	1.11(17)	3.8	1.26(19)	1.0	1.28(11)	2.1
NR	1.56(12)	—	1.66(9)	—	1.50(12)	—	2.05(10)	—

TABLE IV. Extra scale factor N_{TL} needed to fit the experimental R^{TL} response. These factors would multiply those in Table III to scale theory to experiment on R^{TL} . A value of one indicates that no extra enhancement or quenching of the response is found. The numbers in parentheses show the statistical error only. The quality of the fit (χ^2/dof) is also quoted in every case. NR corresponds to the nonrelativistic analysis of ref. [22]. These numbers correspond to EDAI-O potential. Very similar numbers are obtained with EDAD-1, EDAD-2 or EDAD-3.

REFERENCES

- [1] S. Boffi, C. Giusti, F.D. Pacati, Phys. Rep. **226**, 1 (1993); S. Boffi, C. Giusti, F. Pacati, M. Radici, “*Electromagnetic Response of Atomic Nuclei*”, (Oxford-Clarendon Press, 1996); J.J. Kelly, Adv. Nucl. Phys. **23**, 75 (1996).
- [2] I. Bobeldijk *et al.*, Phys. Rev. Lett. **73**, 2684 (1994).
- [3] L. Lapidás, Nucl. Phys. **A553**, 297c (1993).
- [4] A. Meucci, C. Giusti, F. Pacati, nucl.-th/0101034 (Jan. 2001)
- [5] J.M. Udías, P. Sarriguren, E. Moya de Guerra, E. Garrido, J.A. Caballero, Phys. Rev. C **48**, 2731 (1993).
- [6] J.M. Udías, P. Sarriguren, E. Moya de Guerra, E. Garrido, J.A. Caballero, Phys. Rev. C **51**, 3246 (1995).
- [7] J.M. Udías, P. Sarriguren, E. Moya de Guerra, J.A. Caballero, Phys. Rev. C **53**, R1488 (1996).
- [8] J.M. Udías, J.A. Caballero, E. Moya de Guerra, J.E. Amaro, T.W. Donnelly, Phys. Rev. Lett. **83**, 5451 (1999).
- [9] A. Picklesimer, J.W. Van Orden, Phys. Rev. C **35**, 266 (1987); **40**, 290 (1989).
- [10] Y. Jin, D.S. Onley, Phys. Rev. C **50**, 377 (1994).
- [11] S.Gardner, J.Piekarewicz, Phys.Rev. C **50**, 2882 (1994).
- [12] C.J. Horowitz, D.P. Murdock, B.D. Serot, *Computational Nuclear Physics*, Eds. K. Langanke, J.A. Maruhn, S.E. Koonin (Springer, Berlin, 1991).
- [13] E.D. Cooper, S. Hama, B.C. Clark, R.L. Mercer, Phys. Rev. C **47**, 297 (1993).
- [14] J.E. Amaro, J.A. Caballero, T.W. Donnelly, A.M. Lallena, E. Moya de Guerra, J.M. Udías, Nucl. Phys. **A602**, 263 (1996); J.E. Amaro, J.A. Caballero, T.W. Donnelly, E. Moya de Guerra, **A611**, 163 (1996).
- [15] J. Gao *et al.*, Phys. Rev. Lett. **84**, 3265 (2000).
- [16] J.P. McDermott, Phys. Rev. Lett. **65**, 1991 (1990); Y. Jin, D.S. Onley, L.E. Wright, Phys. Rev. C **45**, 1311 (1992).
- [17] J.A. Caballero, T.W. Donnelly, E. Moya de Guerra, J.M. Udías, Nucl. Phys. **A632**, 323 (1998).
- [18] J.A. Caballero, T.W. Donnelly, E. Moya de Guerra, J.M. Udías, Nucl. Phys. **A643**, 189 (1998).
- [19] R.J. Woo *et al.*, Phys. Rev. Lett. **80**, 456 (1998).
- [20] J.M. Udías, J.R. Vignote, Phys. Rev. C **62**, 034302 (2000).
- [21] L. Chinitz *et al.*, Phys. Rev. Lett. **67**, 568 (1991).
- [22] C.M. Spaltro, H.P. Blok, E. Jans, L. Lapidás, M. van der Schaar, G. van der Steenhoven, P.K.A. de Witt Huberts, Phys. Rev. C **48**, 2385 (1993).
- [23] M. Leuschner *et al.*, Phys. Rev. C **49**, 955 (1994).
- [24] P. Schwandt, H.O. Meyer, W.W. Jacobs, A.D. Bacher, S.E. Vigdor, M.D. Kaitchuck, T.R. Donoghue, Phys. Rev. C **26**, 55 (1982).
- [25] V. Van der Sluys, J. Ryckebusch, M. Waroquier, Phys. Rev. C **54**, 1322 (1996).
- [26] J.E. Amaro, A.M. Lallena, J.A. Caballero, Phys. Rev. C **60**, 014602 (1999).
- [27] A.S. Raskin, T.W. Donnelly, Ann. of Phys. (NY) **191**, 78 (1989).
- [28] J.E. Amaro, T.W. Donnelly, Ann. Phys. (NY) **263**, 56 (1998); Nucl. Phys. **A646**, 187 (1999).
- [29] T. de Forest, Nucl. Phys. **A392**, 232 (1983).

- [30] H. Überall, *Electron Scattering from Complex Nuclei*, Academic, N.Y., (1971). M.E. Rose, *Relativistic Electron Scattering*, Wiley, N.Y., (1961).
- [31] B.D. Serot, J.D. Walecka, *Adv. Nucl. Phys.* **16**, 1 (1986).
- [32] J.A. Caballero, T.W. Donnelly, G.I. Poulis, *Nucl. Phys.* **A555**, 709 (1993).
- [33] J.D. Bjorken, S.D. Drell, *Relativistic Quantum Mechanics*, Mc Graw-Hill, N.Y., (1964)
- [34] C. Giusti, F. Pacati, *Nucl. Phys.* **A473**, 717 (1987).
- [35] S. Jeschonnek, T.W. Donnelly, *Phys. Rev. C* **57**, 2438 (1998); S. Jeschonnek, *Phys. Rev. C* **63**, 034609 (2001); S. Jeschonnek, J.W. Van Orden, *Phys. Rev. C* **62**, 044613 (2000).
- [36] G.H. Rawitscher, *Phys. Rev. C* **31**, 1173 (1985).
- [37] S. Boffi, C. Giusti, F.D. Pacati, F. Cannata, *Nuovo Cimento* **98**, 291 (1987).
- [38] M. Hedayati-Poor, J.I. Johansson, H.S. Sherif, *Phys. Rev. C* **51**, 2044 (1995); *Nucl. Phys.* **A593**, 377 (1995); J.I. Johansson, H.S. Sherif, G.M. Lotz, *Nucl. Phys.* **A605**, 517 (1996).
- [39] J.J. Kelly, *Phys. Rev. C* **56**, 2672 (1997); **59**, 3256 (1999).
- [40] H.W.L. Naus, S. Pollock, J.H. Koch, U. Oelfke, *Nucl. Phys.* **A509**, 717 (1990); S. Pollock, H.W.L. Naus, J.H. Koch *Phys. Rev. C* **53**, 2304 (1996).
- [41] M.M. Sharma, M.A. Nagarajan, P. Ring; *Phys. Lett. B* **312**, 377 (1993).
- [42] G.A. Lalazissis, J. König, P. Ring, *Phys. Rev. C* **55**, 540 (1997).
- [43] J.J. Kelly *et al.*, *Phys. Rev. C* **39**, 1222 (1989); J.J. Kelly, *Phys. Rev. C* **39**, 2120 (1989); J.J. Kelly *et al.* *Phys. Rev. C* **41**, 2504 (1990); Q. Cheng, J.J. Kelly, P.P. Singh, M.C. Radhakrishma, W. P. Jones and H. Nann, *Phys. Rev. C* **41**, 2514 (1990); R.S. Flanders *et al.*, *Phys. Rev. C* **43**, 2103 (1991).
- [44] L. Chinitz, Ph.D. Thesis, University of Virginia (1990) (*unpublished*).
- [45] C.M. Spaltro, M.Sc. Thesis, University of Utrecht (1992) (*unpublished*).
- [46] T. Otsuka in “Proceedings of the International NATO-Advanced Study Institute on Nuclei far from Stability and Astrophysics”, Poenareau, Rebel, and Wentz, eds. (NATO-ASI Series, 2000), *in press*.
- [47] D. Van Neck, M. Waroquier, A.E.L. Dieperink, Steven C. Pieper, V.R. Pandharipande, *Phys. Rev. C* **57**, 2308 (1998).
- [48] W.J.W. Geurts, K. Allaart, W.H. Dickhoff and H. Müther, *Phys. Rev. C* **53**, 2207 (1996); H. Müther, W.H. Dickhoff, *Phys. Rev. C* **49**, R17 (1994).
- [49] J. Ryckebusch, D. Debruyne, W.V. Nespén, S. Janssen, *Phys. Rev. C* **60**, 034604 (1999).

FIGURES

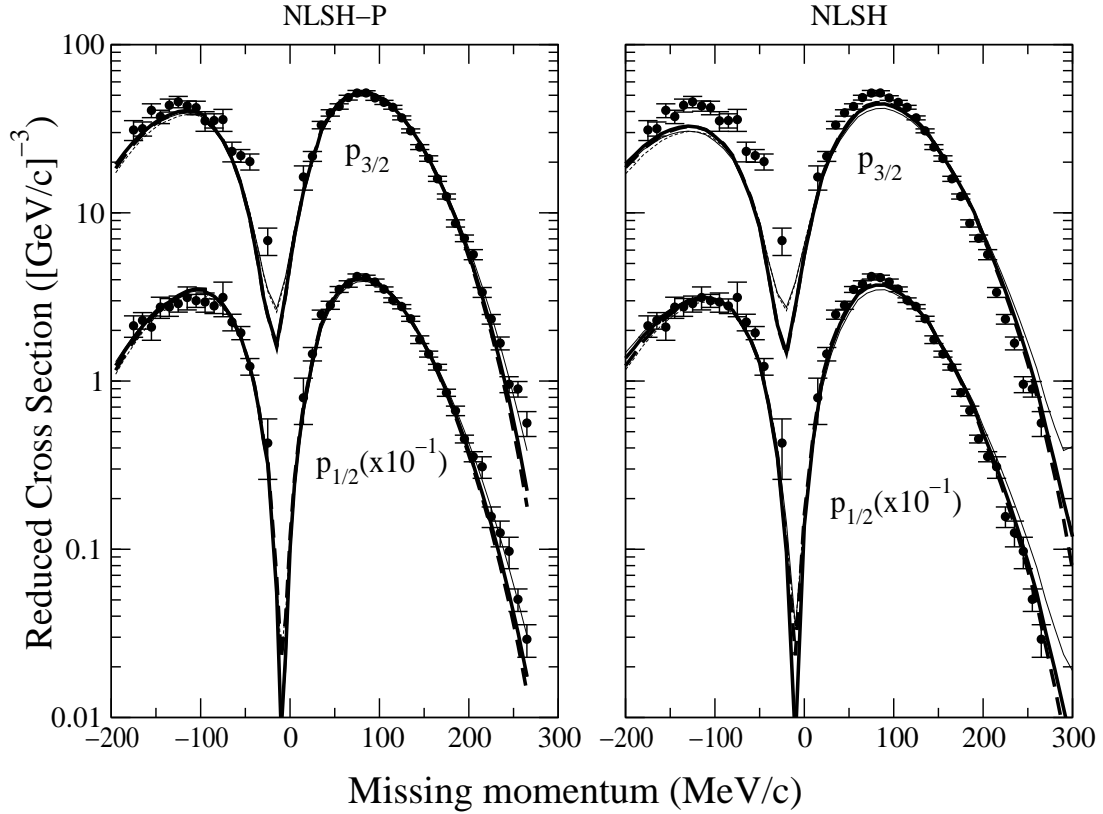


FIG. 1. Reduced cross-sections for proton knockout from $1p_{1/2}$ and $1p_{3/2}$ orbits in ^{16}O versus missing momentum p_m corresponding to the experiment performed by Leuschner *et al.* [23] (set (a)). The bound relativistic proton wave function has been obtained with the NLSH (right panel) and NLSH-P (left panel) parameterization. Theoretical results shown correspond to a fully relativistic calculation using the Coulomb gauge and current operators RCC1 (thin solid line) and RCC2 (thick solid line). The optical potential used is EDAL-O from ref. [13]. Also shown are the results after projecting the bound and scattered proton wave functions over positive-energy states: PCC1 (thin dashed line), PCC2 (thick dashed line). EMA-noSV results (not shown) are practically identical to PCC2 ones. Each curve is scaled by the corresponding spectroscopic factor in Table I.

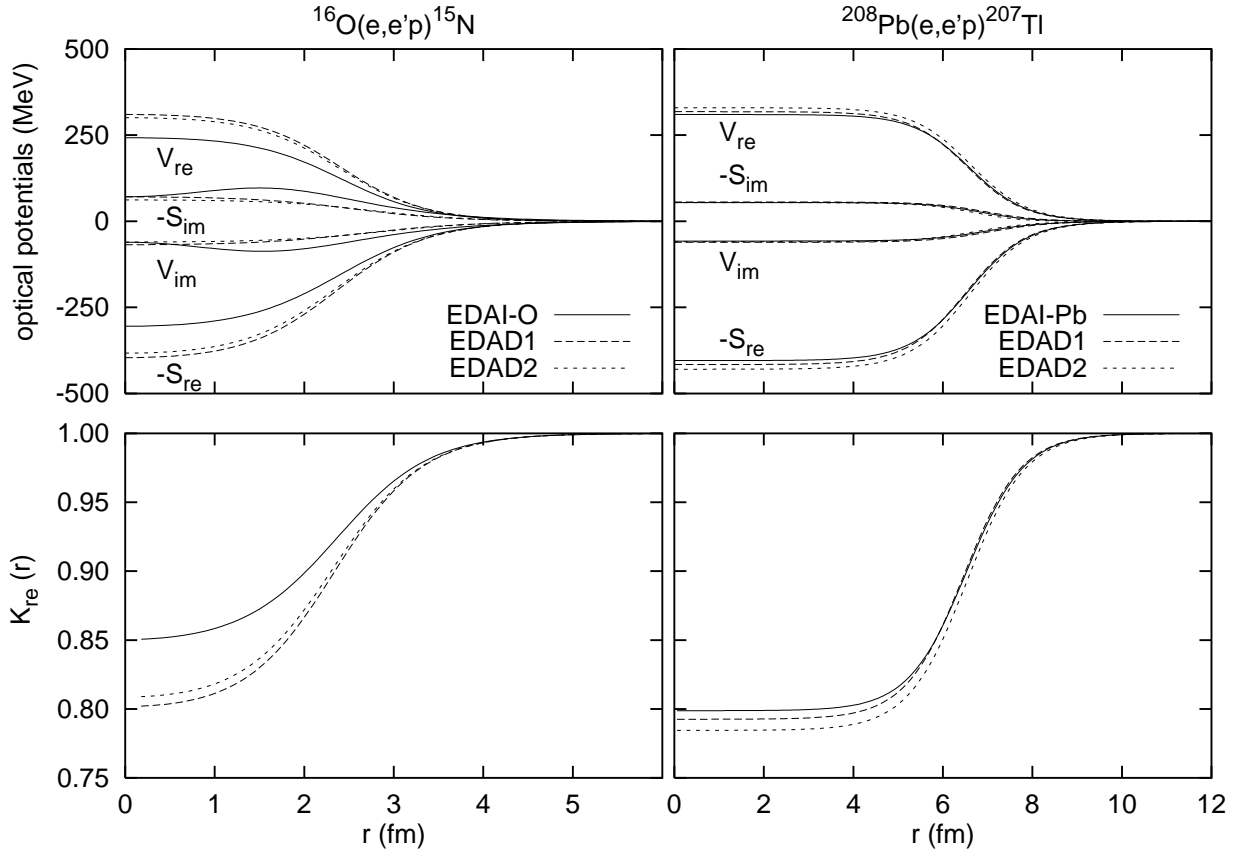


FIG. 2. Real and imaginary part of the optical potentials (upper panels) and real part of the Darwin factor (lower panels) (the imaginary part is negligible) for ^{16}O (left panels) and ^{208}Pb (right panels).

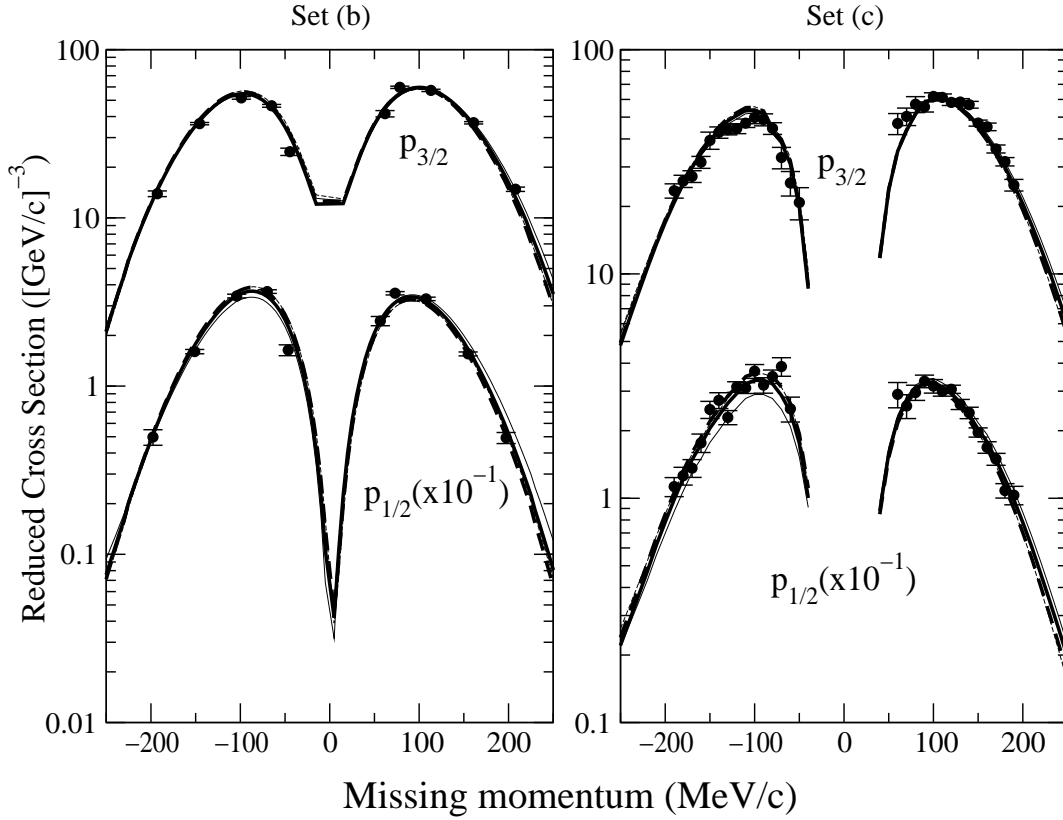


FIG. 3. Same as Fig. 1 for the experiments performed by Chinitz *et al.* [21] (left panel, set (b)) and by Spaltro *et al.* [22] (right panel, set (c)). In all the cases the NLSH-P relativistic bound proton wave function and EDAI-O optical potential has been used. For $p_{3/2}$ shell in set (b) the contribution from the nearby $5/2^+$ and $1/2^+$ states has been taken into account (see text). Each curve is scaled by the corresponding spectroscopic factor in Table III.

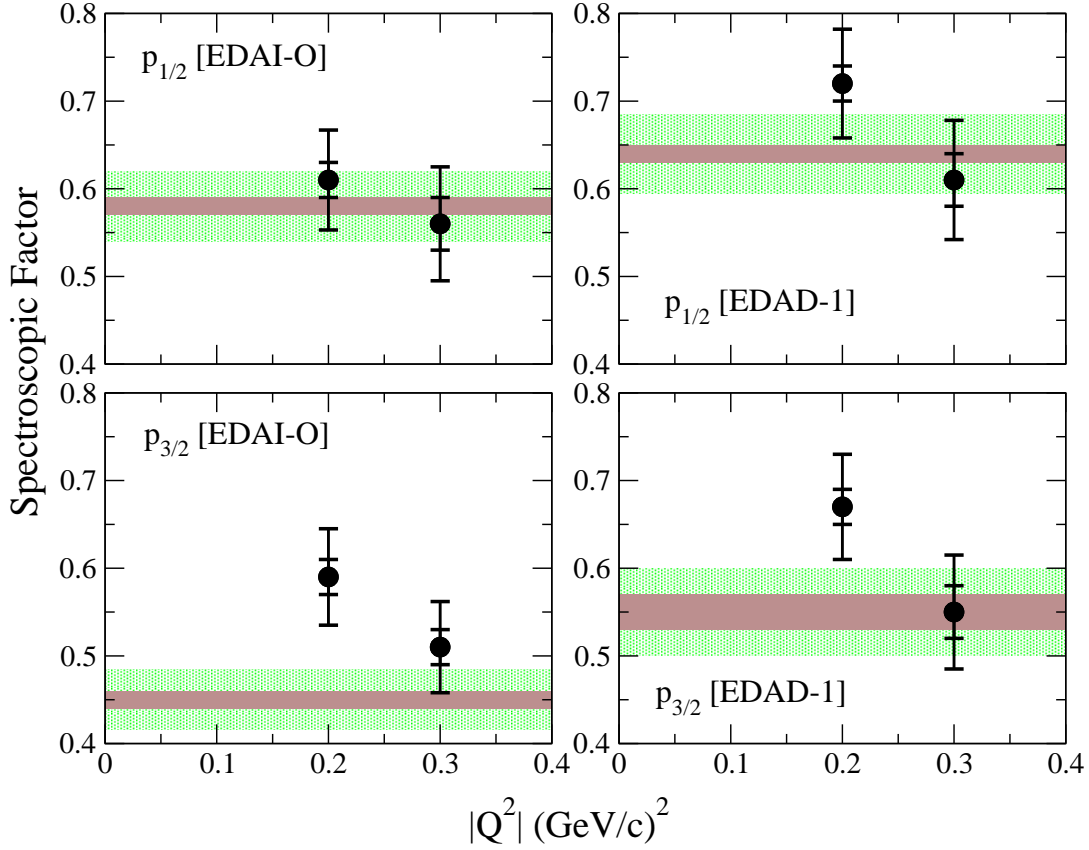


FIG. 4. Spectroscopic factors derived within the fully relativistic approach from the low- Q^2 data discussed in this work with NLSH-P wave function, CC2 current operator and EDAI-O (left) or EDAD-1 (right) optical potentials. The inner error bars include statistical errors only, the outer one includes also the additional systematic error in the reduced cross-sections for each experiment. The bands covering the whole $|Q^2|$ range corresponds to the value obtained from the data set (a) [23], while the dots at $|Q^2| = 0.2$ (GeV/c) 2 and 0.3 (GeV/c) 2 correspond to the data set (c) [22] and set (b) [21], respectively.

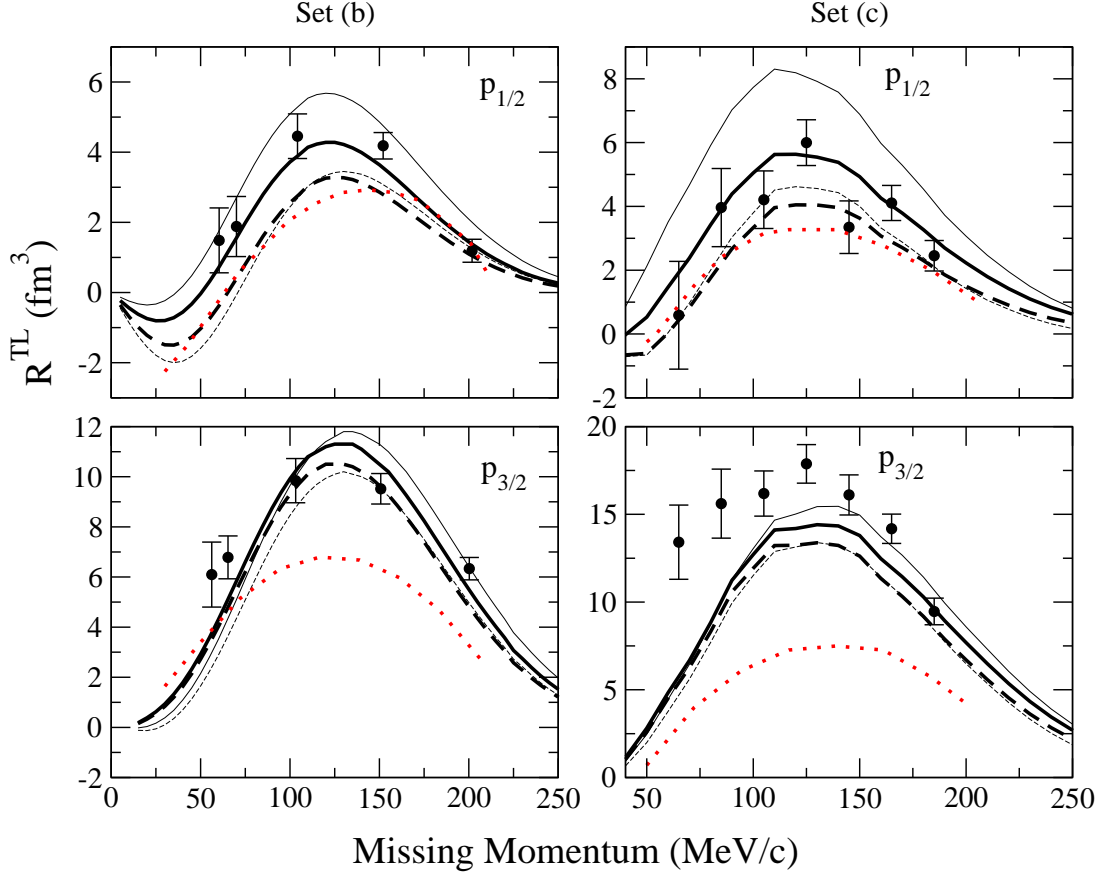


FIG. 5. Response R^{TL} for proton knockout from ^{16}O for $1p_{1/2}$ (top panels) and $1p_{3/2}$ (bottom panels). Results and data shown correspond to kinematics of data set (b) [21] (left) and set (c) [22] (right). Line conventions as in Figs. 1 and 3 (NLSH-P wave function and EDAI-O optical potential). The curves have been scaled by the spectroscopic factors in Table III. Additional dotted curves correspond to the nonrelativistic analyses of ref. [22].

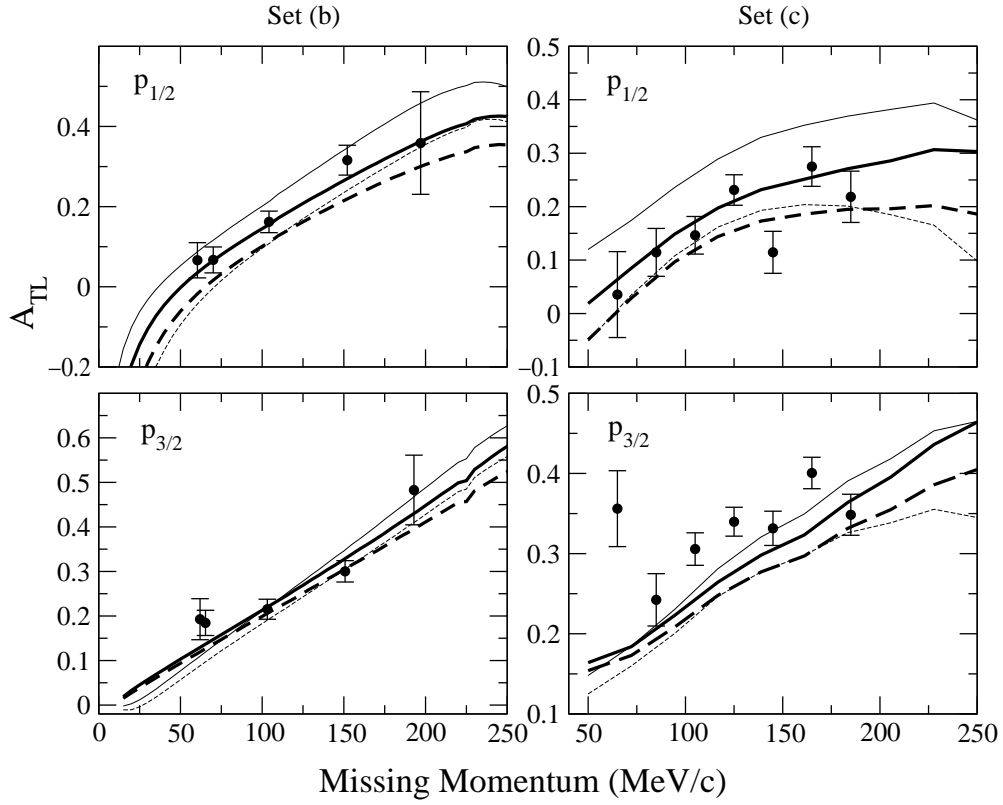


FIG. 6. Same as Fig. 5 for the A_{TL} asymmetry. We recall that this observable is independent on the spectroscopic factor.

Set (c) kinematics

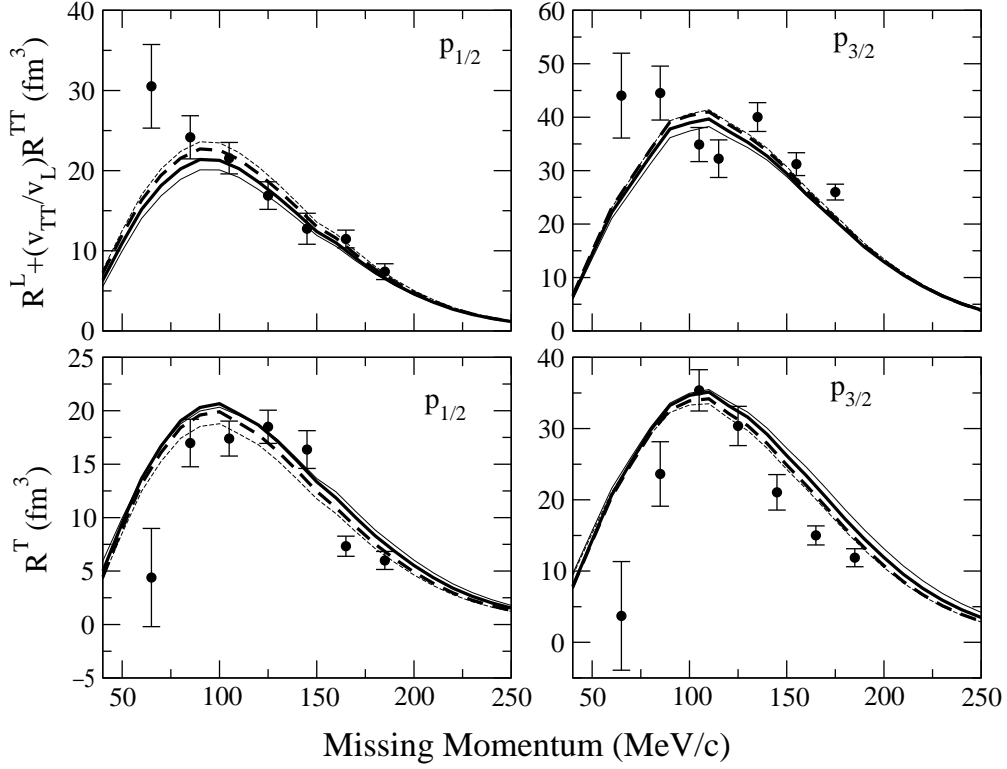


FIG. 7. Response functions $R^L + v_{TT}/v_L R^{TT}$ and R^T for the kinematics of data set (c) [22]. Curves and calculations as in Fig. 3. The theoretical results are scaled with spectroscopic factors for this same experiment in Table III.